JACS
JOURNAL OF THE AMERICAN CHEMICAL SOCIETY
pubs.acs.org/JACS
Article

Hydrogen Radical-Induced Electrocatalytic N_2 Reduction at a Low Potential

Xueting Feng,[⊥] Jiyuan Liu,[⊥] Long Chen, Ya Kong, Zedong Zhang, Zixuan Zhang, Dingsheng Wang, Wen Liu, Shuzhou Li,* Lianming Tong,* and Jin Zhang*

Cite This: J. Am. Chem. Soc. 2023, 145, 10259−10267

Read Online

ACCESS | Metrics & More | Article Recommendations | Supporting Information

ABSTRACT: Realizing efficient hydrogenation of N_2 molecules in the electrocatalytic nitrogen reduction reaction (NRR) is crucial in achieving high activity at a low potential because it theoretically requires a higher equilibrium potential than other steps. Analogous to metal hydride complexes for N_2 reduction, achieving this step by chemical hydrogenation can weaken the potential dependence of the initial hydrogenation process. However, this strategy is rarely reported in the electrocatalytic NRR, and the catalytic mechanism remains ambiguous and lacks experimental evidence. Here, we show a highly efficient electrocatalyst (ruthenium single atoms anchored on graphdiyne/graphene sandwich structures) with a hydrogen radical-transferring mechanism, in which graphdiyne (GDY) generates hydrogen radicals (H•), which can effectively activate N_2 to generate NNH radicals (•NNH). A dual-active site is constructed to suppress competing hydrogen evolution, where hydrogen preferentially adsorbs on GDY and Ru single atoms serve as the adsorption site of •NNH to promote further hydrogenation of NH_3 synthesis. As a result, high activity and selectivity are obtained simultaneously at −0.1 V versus a reversible hydrogen electrode. Our findings illustrate a novel hydrogen transfer mechanism that can greatly reduce the potential and maintain the high activity and selectivity in NRR and provide powerful guidelines for the design concept of electrocatalysts.

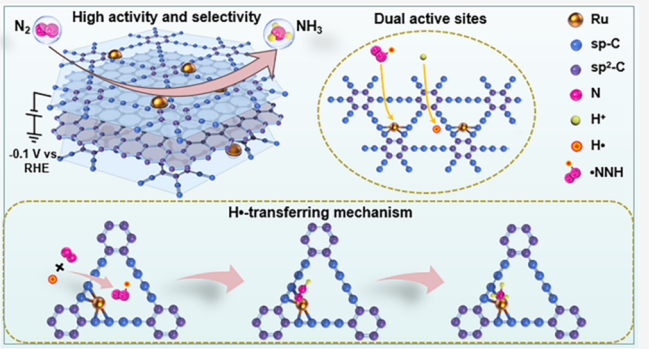

INTRODUCTION

Electrocatalytic NRR generally suffers from poor NH_3 selectivity and activity due to the competitive hydrogen evolution and high reaction barrier.[1,2] From the thermodynamic perspective, it typically proceeds at a potential similar to that required for the hydrogen evolution reaction (HER), accounting for the extremely low Faradaic efficiency (FE) toward NH_3 synthesis.[3−5] Especially at a large potential, HER is more likely to occur. From the kinetic view, the formation of *NNH (* represents the catalyst surface sites), which is widely considered as a rate-limiting step, limits the improvement of NRR activity due to its relatively large energy barrier.[6−9] Accordingly, it is imperative to construct an electrocatalyst that could balance the competition between H and N_2 on the active site and accelerate the reaction kinetics of the hydrogenation process, thereby enhancing the NRR activity at a low potential. As shown in Figure 1a, an NRR electrocatalyst of Ru single atoms (Ru SAs) on graphdiyne/graphene sandwich structures (GDY/G) is designed. Ru, as a second-generation NH_3 catalyst, has shown high activity toward NRR due to the appropriate N_2 adsorption energy and required potential much lower than that of other precious metals.[10,11] Recently, single-atom catalysts with atomically dispersed metal active centers have attracted extensive research interest due to their maximum atomic efficiency.[12] These catalysts have well-defined active sites, providing a unique opportunity to further understand the reaction mechanism on the active sites.[13] Due to the unique atomic structures and electronic properties, single-atom catalysts exhibit extremely excellent catalytic activity and selectivity in many electrocatalytic reactions.[14,15] For example, Ru single-atom catalysts enable high FE due to the lower adsorption capacity of H than that on metal particles or clusters.[16,17] Graphdiyne (GDY), a carbon allotrope composed of sp^2 and sp hybrid carbon atoms, has high intrinsic activity for HER due to uneven surface charge distribution compared with several other carbon materials, such as graphene, carbon nanotubes, and fullerenes.[18,19] Thus, an electrocatalyst with dual-active sites is constructed, where the H adsorption and N_2 hydrogenation process take place at spatially separated sites separately. Here, the H^+ preferentially attacks GDY rather than Ru single atoms, effectively inhibiting

Received: February 5, 2023
Published: April 25, 2023

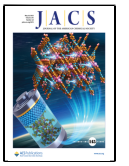

https://doi.org/10.1021/jacs.3c01319
J. Am. Chem. Soc. 2023, 145, 10259−10267

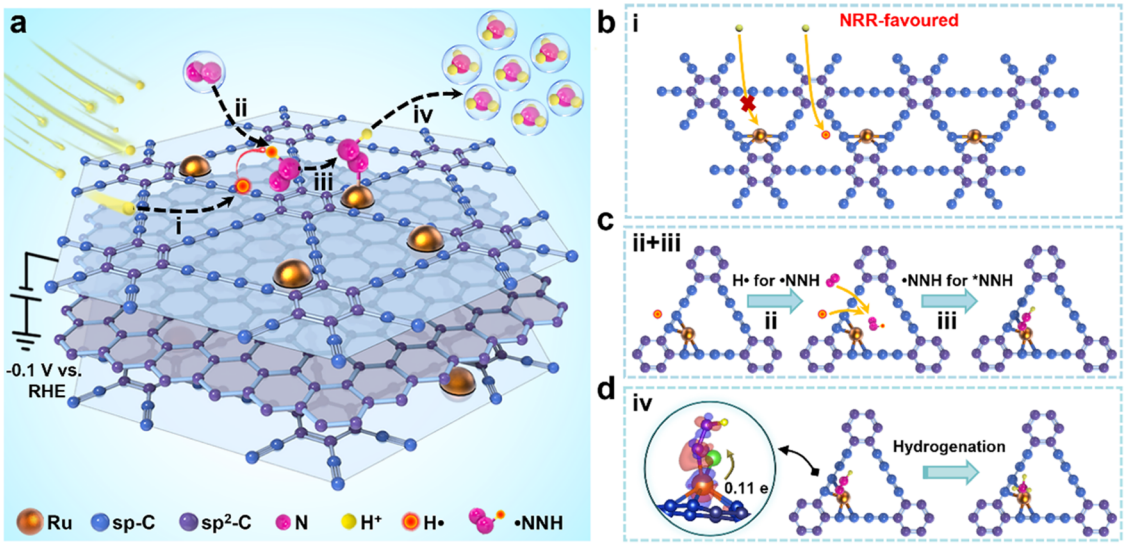

Figure 1. Conceptual diagram of N_2 electroreduction to ammonia (NH_3) on Ru SAs/GDY/G. Ru SAs/GDY/G stands for ruthenium single atoms (Ru SAs) anchored on graphdiyne/graphene sandwich structures (GDY/G). (a) Proposed reaction scheme for N_2 electroreduction to NH_3 on Ru SAs/GDY/G. (b) Mass transfer of protons to the Ru SAs/GDY/G surface in electrolytes. (c) Schematic representation of the •NNH generation mechanism and *NNH adsorption configurations on Ru single atoms. (d) Hydrogenation of NH_3 synthesis on Ru single atoms and the charge density fluctuations of *NNH adsorption configurations (charge density accumulation and depletion depicted in orange and blue, respectively).

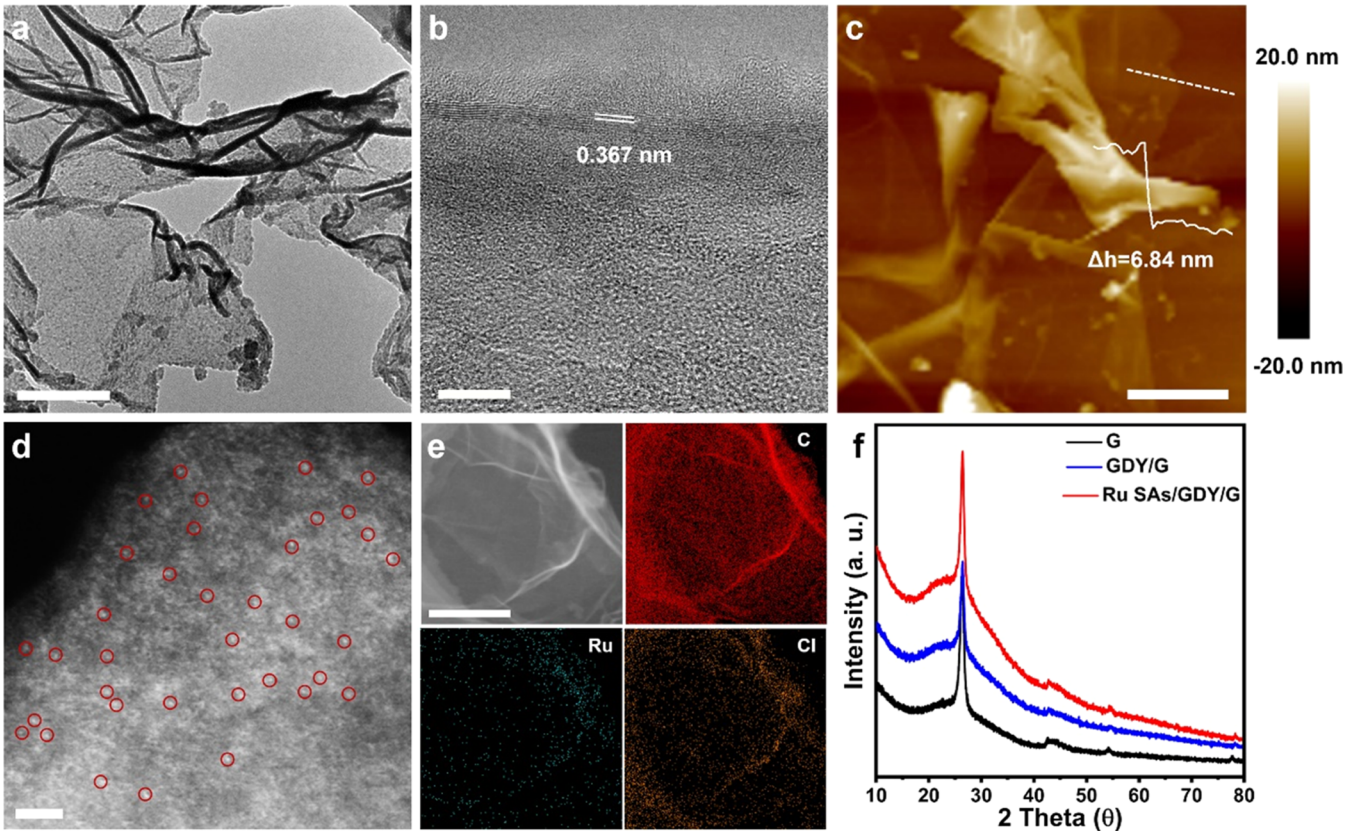

Figure 2. Characterizations of GDY/G and Ru SAs/GDY/G. GDY/G stands for graphdiyne/graphene sandwich structures. (a) Transmission electron microscopy (TEM) image of GDY/G. Scale bar, 500 nm. (b) High-resolution TEM (HRTEM) image of GDY/G. Scale bar, 10 nm. (c) Atomic force microscopy (AFM) image of GDY/G. Scale bar, 500 nm. (d) Aberration-corrected high-angle annular dark-field scanning transmission electron microscopy (HAADF-STEM) image of Ru SAs/GDY/G. Some of Ru single atoms are indicated by the red circles. Scale bar, 2 nm. (e) HAADF-STEM image and corresponding EDX elemental mapping images of Ru SAs/GDY/G, C (red), Ru (cyan), and Cl (orange). Scale bar, 300 nm. (f) X-ray diffraction (XRD) patterns of Ru SAs/GDY/G, GDY/G, and G. G stands for a graphene sheet.

the coverage of H at the Ru active sites, thus improving the FE of the NRR process (Figure 1b). Furthermore, we show that the GDY can generate hydrogen radicals ($H^•$), and a new mechanism via a $H^•$ transfer pathway is proposed that

https://doi.org/10.1021/jacs.3c01319
J. Am. Chem. Soc. 2023, 145, 10259−10267

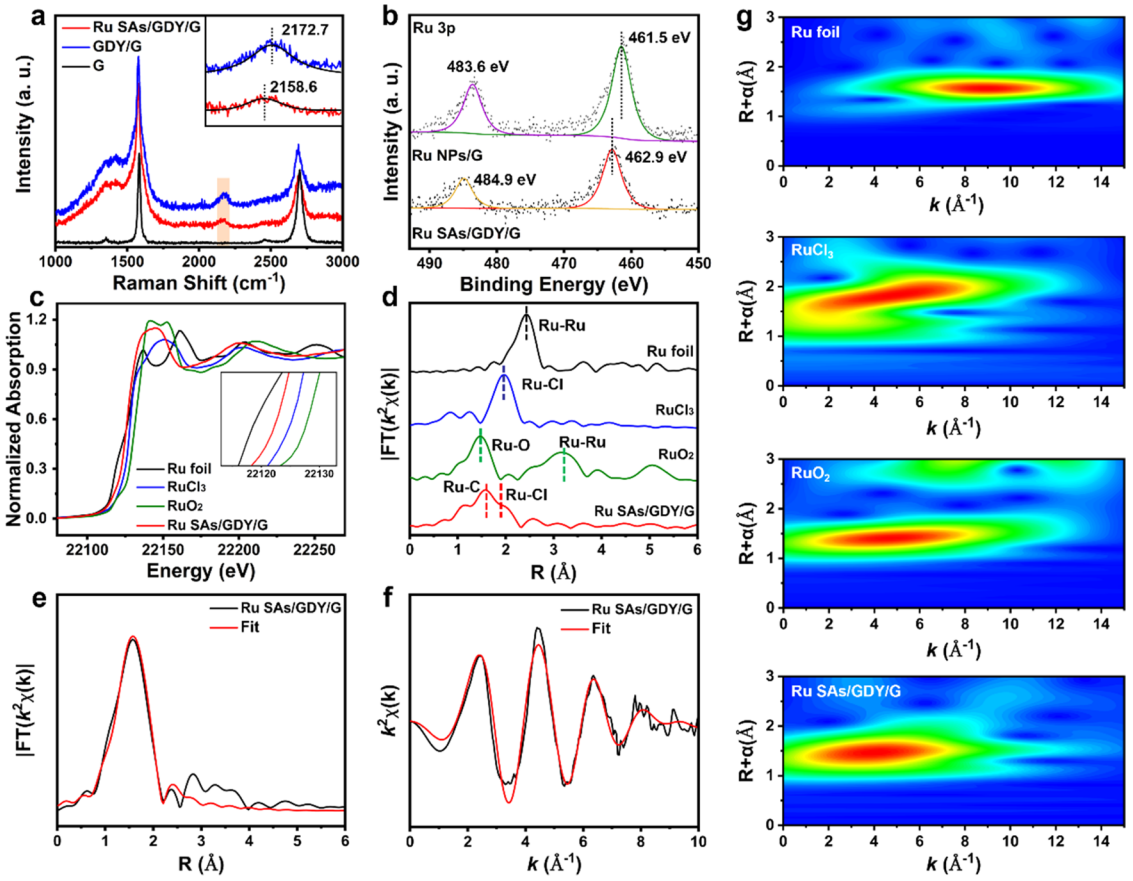

Figure 3. Structural analysis of Ru SAs/GDY/G. (a) Raman spectra of Ru SAs/GDY/G, GDY/G, and G. (b) High-resolution Ru 3p XPS spectra of Ru SAs/GDY/G and Ru NPs/G. Ru NPs/G stands for ruthenium nanoparticles on the graphene sheet. (c) X-ray absorption near-edge structure (XANES) spectra and (d) Fourier-transformed (FT) k^2-weighted $\chi(k)$-function of the EXAFS spectra at the Ru K-edge of Ru SAs/GDY/G, referenced Ru foil, $RuCl_3$, and RuO_2. (e) EXAFS fitting curves of Ru SAs/GDY/G at the R space. (f) EXAFS fitting curves of Ru SAs/GDY/G at the k space. (g) Wavelet transform (WT) for the k^2-weighted EXAFS signals of the Ru K-edge.

expedites the reaction kinetics of the hydrogenation process. In brief, the combined effect of both the dual-active sites and the H•-transferring mechanism leads to high activity and selectivity simultaneously on the Ru SAs/GDY/G catalyst at a low potential (−0.1 V versus a reversible hydrogen electrode).

The whole design concept of NRR on the Ru SAs/GDY/G catalyst goes through the following steps (Figure 1a). The GDY can generate H• (step i). H• can react with N_2 to form NNH radicals (•NNH), and then the •NNH adsorbs on Ru single atoms to form *NNH (steps ii and iii in Figure 1c). Subsequently, *NNH goes through a step-by-step hydrogenation to form *NH_3 and then desorbs to form NH_3 (step iv in Figure 1d).

RESULTS AND DISCUSSION

Synthesis and Characterization of Catalysts. The Ru SAs/GDY/G catalyst was synthesized through a simple impregnation method on the graphdiyne/graphene sandwich structures (Supporting Figure S1). Briefly, the GDY/G was fabricated via an Eglinton coupling reaction using a fast, simple, and efficient microwave synthesis.[20] This strategy involves mixing $Cu(OAc)_2{\cdot}H_2O$ and graphene with monomer hexaethynylbenzene (HEB) at room temperature, followed by microwave radiation of the mixture for only 1 min in a household microwave oven. The photograph of as-prepared GDY/G powder is shown in Supporting Figure S2a. X-ray photoelectron spectroscopy (XPS) and inductively coupled plasma mass spectrometry (ICP-MS) analysis confirm that only a very small amount of copper remains in the GDY/G, with a content of 0.16 wt % (Supporting Figure S2b). The residual copper has no effect on electrocatalytic performance, which will be discussed later in this work. The XPS C 1s spectrum of GDY/G is deconvoluted into four peaks at 284.4, 285.0, 286.4, and 288.5 eV, assigning to C−C (sp^2), C−C (sp), C−O, and C═O, respectively (Supporting Figure S3).[21] From the GDY structural model, the theoretical ratio of sp to sp^2 carbon atoms should be 2. However, the experimentally obtained ratio is less than 2 due to the existence of graphene.[20] The transmission electron microscopy (TEM) image of GDY/G indicates a lamellar structure, in which the smooth surface of graphene is covered by a GDY thin film (Figure 2a and Supporting Figure S4a). The high-resolution TEM (HRTEM) in Supporting Figure S5 shows a well-defined interface between GDY and graphene, further elaborating that the GDY film grows in-plane on graphene. Due to the van der Waals interaction and lattice match between GDY and graphene, the GDY thin film uniformly distributed on both sides of the graphene.[22] In the absence of graphene, the GDY samples obtained by the same strategy are severely stacked (Supporting Figure S6a−c), confirming the importance of graphene as a template in GDY growth. Additionally, the interlayer space of 0.367 nm and 0.366 nm are observed at the edges of the GDY/G and GDY, respectively, which is classified

https://doi.org/10.1021/jacs.3c01319
J. Am. Chem. Soc. 2023, 145, 10259−10267

to the interlayer space of GDY (Figure 2b and Supporting Figure S6d). The atomic force microscopy (AFM) image (Figure 2c) suggests that the thickness of GDY/G is about 6.84 nm, in which the thickness of graphene is 2.74 nm (Supporting Figure S4b). Therefore, it can be calculated that the thickness of the GDY film on the graphene side is about 2.05 nm. Afterward, the Ru SAs/GDY/G was obtained by an impregnation method, and its morphology was first characterized by TEM in Supporting Figure S7. It shows a sandwich-like structure originating from GDY/G, and no obvious Ru nanoparticles or clusters can be observed on the GDY/G scaffold. From aberration-corrected high-angle annular dark-field scanning transmission electron microscopy (HAADF-STEM) (Figure 2d), isolated Ru single atoms anchored on the GDY/G can be clearly assigned as bright dots. The content of Ru is estimated to be 1.8 wt % based on ICP-MS analysis, which is in agreement with the results of energy-dispersive X-ray spectroscopy (EDX) (1.5 wt %, Supporting Figure S8). EDX mapping analysis in Figure 2e reveals the existence of Ru, C, and Cl elements throughout the Ru SAs/GDY/G and the uniform dispersion of Ru element in the GDY/G. The X-ray diffraction (XRD) patterns of Ru SAs/GDY/G in Figure 2f indicate that there are no peaks related to Ru-based crystals, further demonstrating the single-atomic nature of Ru in Ru SAs/GDY/G. The XRD patterns of Ru SAs/GDY/G and GDY/G are similar. A broad peak over 23° corresponds to the interlayer distance of GDY,[23] and two peaks at 26.2° and 54.0° are ascribed to the (002) and (004) planes of graphitic carbon, respectively.[24] For comparison, the Ru nanoparticles on the graphene sheet (Ru NPs/G) control sample was prepared and characterized. ICP-MS analysis shows that the Ru content in the Ru NPs/G is 8.4 wt %. The Ru nanoparticles are distributed in the graphene matrix with a highly agglomerated distribution, and a clearly visible crystal structure of Ru nanoparticles is illustrated in Supporting Figure S9. The corresponding fast Fourier transform (FFT) exhibits that the lattice spacing of 0.214 nm is attributed to the (002) plane of hexagonal Ru. The specific surface area and pore volume of Ru SAs/GDY/G are 211.20 $m^2\ g^{-1}$ and 0.37 $cm^3\ g^{-1}$, respectively, which are higher than those of Ru NPs/G (98.68 $m^2\ g^{-1}$ and 0.26 $cm^3\ g^{-1}$, Supporting Figure S10).

The structure of catalysts was further investigated by Raman spectroscopy, XPS, and X-ray absorption spectroscopy (XAS). Figure 3a shows Raman spectra of Ru SAs/GDY/G, GDY/G, and G. The distinct peaks at approximately 1353.1, 1583.2, and 2701.1 cm^{-1} are assigned as the D band, G band, and 2D band of graphene, respectively. The Y peak centered at 2158.6 and 2172.7 cm^{-1} in the Ru SAs/GDY/G and GDY/G, respectively, is attributed to the triple bond vibration of the diacetylenic linkages (−C≡C−C≡C−) in GDY. The obvious red shift suggests the generation of coordination bonds between Ru and C of the diacetylenic linkages in GDY.[25] XPS analysis shows the presence of oxidized ruthenium on the surface of Ru SAs/GDY/G. In Figure 3b, the binding energies of Ru $3p_{3/2}$ and Ru $3p_{1/2}$ peaks in the Ru SAs/GDY/G are 462.9 and 484.9 eV, respectively, which correspond to the oxidized ruthenium.[26] Correspondingly, the two peaks appeared at 461.5 and 483.6 eV in Ru NPs/G are attributed to the metallic ruthenium.[27] The binding energies of Ru SAs/GDY/G are higher than that of Ru NPs/G and lower than that of Ru^{3+}, indicating that the valence states of Ru in the Ru SAs/GDY/G are between 0 and 3.[26] X-ray absorption fine structure (XAFS) spectroscopy was performed to further reveal the state of the Ru species in the Ru SAs/GDY/G at the atomic level, with Ru foil, $RuCl_3$, and RuO_2 as references. In Figure 3c, the near-edge absorption energy of Ru SAs/GDY/G is situated between Ru foil and $RuCl_3$ references, further implying that the oxidation state of Ru sits between Ru^0 and Ru^{3+}, and the results are consistent with XPS analysis. The comparison of the k^2-weighted EXAFS paths is shown in Supporting Figure S11. The Fourier-transformed k^2-weighted extended XAFS (FT-EXAFS, without phase correction) spectrum of Ru SAs/GDY/G exhibits two distinct peaks at around 1.56 Å and 1.86 Å, assigning to the Ru−C and Ru−Cl superimposed contribution, respectively (Figure 3d).[28,29] No obvious Ru−Ru coordination peak at 2.42 Å and other peaks are observed, demonstrating the atomic dispersion of Ru atoms on GDY/G. Moreover, the Cl 2p XPS spectrum further indicates the existence of Cl in Ru SAs/GDY/G (Supporting Figure S12a). The atomically dispersed Ru sites of Ru SAs/GDY/G were further confirmed by the wavelet transform (WT)-EXAFS due to its high resolution in both R and k spaces.[30] The Ru K-edge WT-EXAFS oscillations in Figure 3g show one intensity maximum at ∼4.1 $Å^{-1}$, which corresponds to the first coordination shell of Ru element (Ru−C and Cl coordination). Compared with the WT plots of Ru foil, $RuCl_3$, and RuO_2 references, no intensity maximum arising from Ru−Ru contribution is observed. The above results directly confirm the dispersion of isolated Ru atoms in Ru SAs/GDY/G. The EXAFS fitting results show that the Ru−C bond length and Ru−Cl bond length are 2.05 Å and 2.34 Å, respectively, revealing that the Ru atoms anchored on GDY/G are coordinated by four C atoms and a Cl atom (Figure 3e,f and Supporting Table S1). The corresponding structure model of Ru SAs/GDY/G is shown in Supporting Figure S12b.

Electrocatalytic N_2 Reduction Performance. The electrochemical nitrogen reduction reaction (NRR) was conducted in a customized H-cell separated by a Nafion 117 membrane at room temperature (Supporting Figure S13). Based on the rigorous experimental protocol, a series of tests were carried out to obtain reliable evidence of NRR activity.[31] The produced ammonia was analyzed and quantified by spectrophotometric and NMR methods. As shown in Supporting Figures S14−S19, no NH_3 and NO_x contaminants are observed in the fully purified gas ($^{14}N_2$ and $^{15}N_2$). Moreover, no NH_3 contaminant was detected in the electrolyte (1) bubbled by purified N_2 or Ar without an applying potential for 1 h, (2) saturated by purified N_2 or Ar under an open-circuit potential (OCP) for 1 h, (3) saturated by purified Ar at different applied potentials for 1 h (Supporting Figures S20 and S21). To assess the NRR performance of catalysts, linear sweep voltammetry (LSV) was carried out in Ar- versus N_2-saturated acidic sodium sulfate electrolytes (pH 2.2, 0.5 M Na_2SO_4), and all potentials were converted to a reversible hydrogen electrode (RHE) by experimental calibration (Supporting Figure S22). Remarkably, the clear differences of current density for Ru SAs/GDY/G can be observed in Ar- and N_2-saturated electrolytes (Supporting Figure S23a), indicating the electrochemical responses for NRR,[32] which is larger than that of Ru NPs/G (Supporting Figure S23b). The NH_3 production and possible byproduct N_2H_4 in the electrolyte were quantified, and no byproduct N_2H_4 was detected during the NRR test (Supporting Figures S24 and S25). Then, chronoamperometry measurements were conducted to further systematically study the NRR activity of Ru SAs/GDY/G with continuous N_2 bubbling (Supporting Figure S26a), and the corresponding UV−vis absorption spectra are

https://doi.org/10.1021/jacs.3c01319
J. Am. Chem. Soc. 2023, 145, 10259−10267

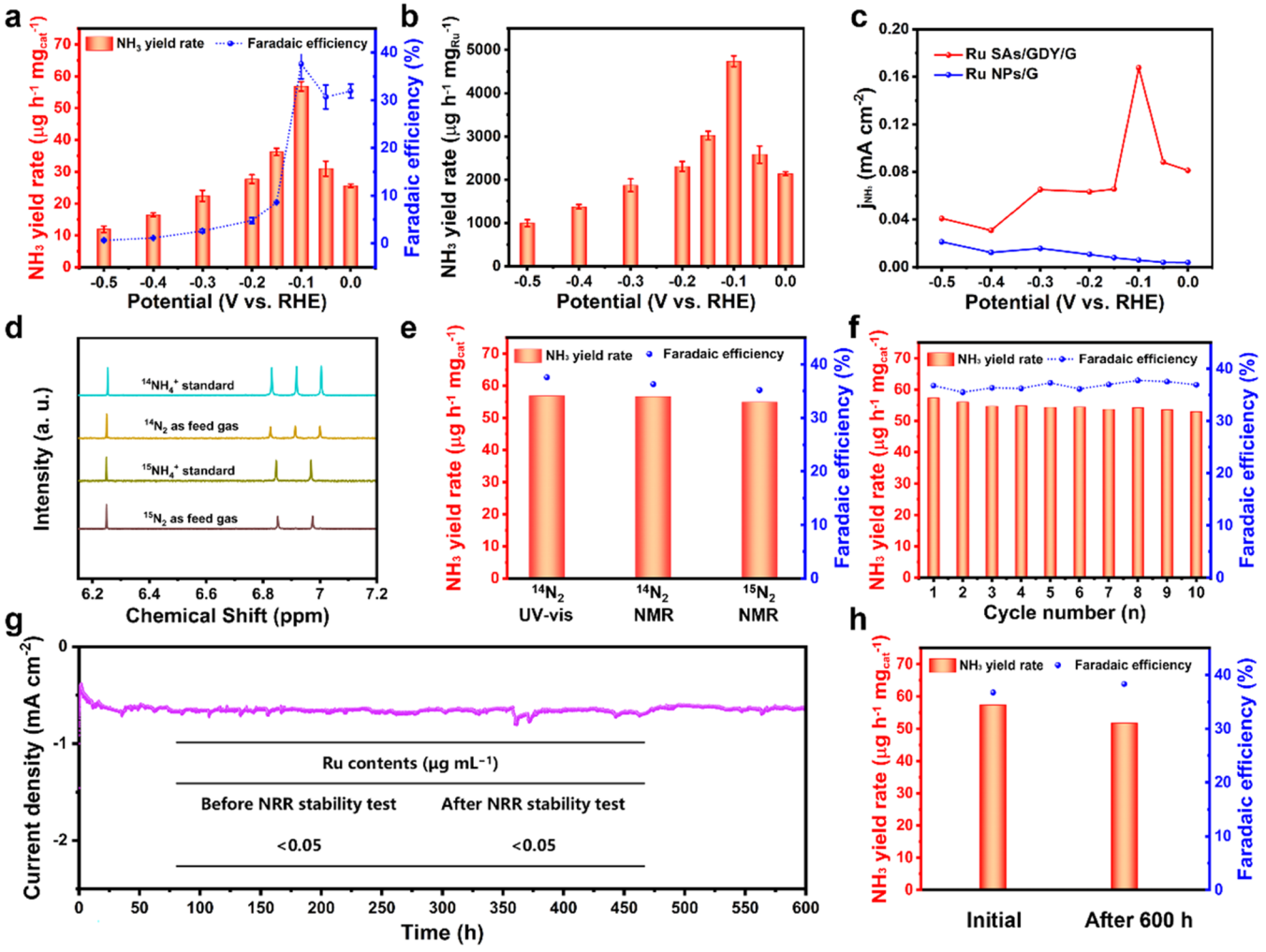

Figure 4. Electroreduction of N_2 to NH_3 under ambient conditions. (a) NH_3 yield rate and Faradaic efficiency (FE) of Ru SAs/GDY/G at selected potentials. (b) NH_3 yield rate normalized by the mass of Ru for Ru SAs/GDY/G at different potentials. (c) Partial current densities (j_{NH3}) of NRR at different applied potentials of Ru SAs/GDY/G and Ru NPs/G. (d) ^1H NMR spectra of the NRR products using different feed gases. (e) Comparison of the calculated NH_3 yield rate and FE at −0.1 V by NMR and UV−vis methods. (f) Cycling test and (g) stability test of Ru SAs/GDY/G at −0.1 V. Inset: Ru contents in electrolytes before and after 600 h stability. (h) NH_3 yield rate and FE of initial and after 600 h stability test.

shown in Supporting Figure S26b. The average NH_3 yield rate and FE of Ru SAs/GDY/G are exhibited in Figure 4a. Strikingly, the highest NH_3 yield rate of 56.8 $\mu g\ h^{-1}\ mg_{cat.}^{-1}$ (4.7 $mg\ h^{-1} mg_{Ru}^{-1}$) with an FE of 37.6% was achieved at an applied potential of −0.1 V vs RHE, nearly 6.1 and 5.0 times than those of Ru NPs/G, respectively (Figure 4b and Supporting Figure S27). Such an NH_3 yield rate and selectivity achieved simultaneously at a low potential outperforms most of previously reported work (Supporting Table S2). Additionally, the NRR activity of Ru SAs/GDY/G was also evaluated in 0.5 M Na_2SO_4 and 0.1 M KOH. As shown in Supporting Figure S28, the Ru SAs/GDY/G catalyst exhibits a remarkable NH_3 yield rate of 57.6 $\mu g\ h^{-1}\ mg_{cat.}^{-1}$ at −0.15 V and FE of 31.5% at −0.1 V in 0.5 M Na_2SO_4, and shows a maximum NH_3 yield rate of 60.1 $\mu g\ h^{-1}\ mg_{cat.}^{-1}$ at −0.2 V and FE of 32.4% at 0 V in 0.1 M KOH. From the above results, it is found that the Ru SAs/GDY/G catalyst can effectively catalyze the NRR in acidic sodium sulfate electrolytes, 0.5 M Na_2SO_4 and 0.1 M KOH, and the required potential is the lowest in acidic sodium sulfate electrolytes. As shown in Figure 4c, the highest partial current density of 0.17 mA cm^{-2} over the Ru SAs/GDY/G catalyst is almost 8 times than that of the Ru NPs/G (0.02 mA cm^{-2}). Interestingly, sole GDY/G shows no detectable NH_3 production at different applied potentials (Supporting Figure S29a), whereas anchoring Ru single atoms on GDY/G promote the NRR significantly, indicating that GDY/G is inert for the NRR process and the single-atom-dispersed Ru is regarded as a main active site for NRR. Additionally, we also evaluated the NRR performance of GDY/G at different pH values, showing almost no NH_3 formation (Supporting Figure S29b,c). Thus, we conclude that the residual copper in GDY/G has no effect on electrocatalytic NH_3 production. For further confirmation of the N source and accurate quantification of the NH_3 product from Ru SAs/GDY/G during NRR, isotope-labeling experiments were performed. The ^1H nuclear magnetic resonance (NMR) spectra show that a doublet signal corresponding to $^{15}NH_4^+$ and triple signal representing $^{14}NH_4^+$ are observed when using $^{15}N_2$ and $^{14}N_2$ as gas supply, respectively, revealing that the feeding gas is the only N source (Figure 4d). The NH_3 yield rate and FE determined by NMR are 56.6 $\mu g\ h^{-1}\ mg_{cat.}^{-1}$ and 36.3% using $^{14}N_2$ as gas and 54.9 $\mu g\ h^{-1}\ mg_{cat.}^{-1}$ and 35.2% using $^{15}N_2$ as gas at −0.1 V for Ru

https://doi.org/10.1021/jacs.3c01319
J. Am. Chem. Soc. 2023, 145, 10259−10267

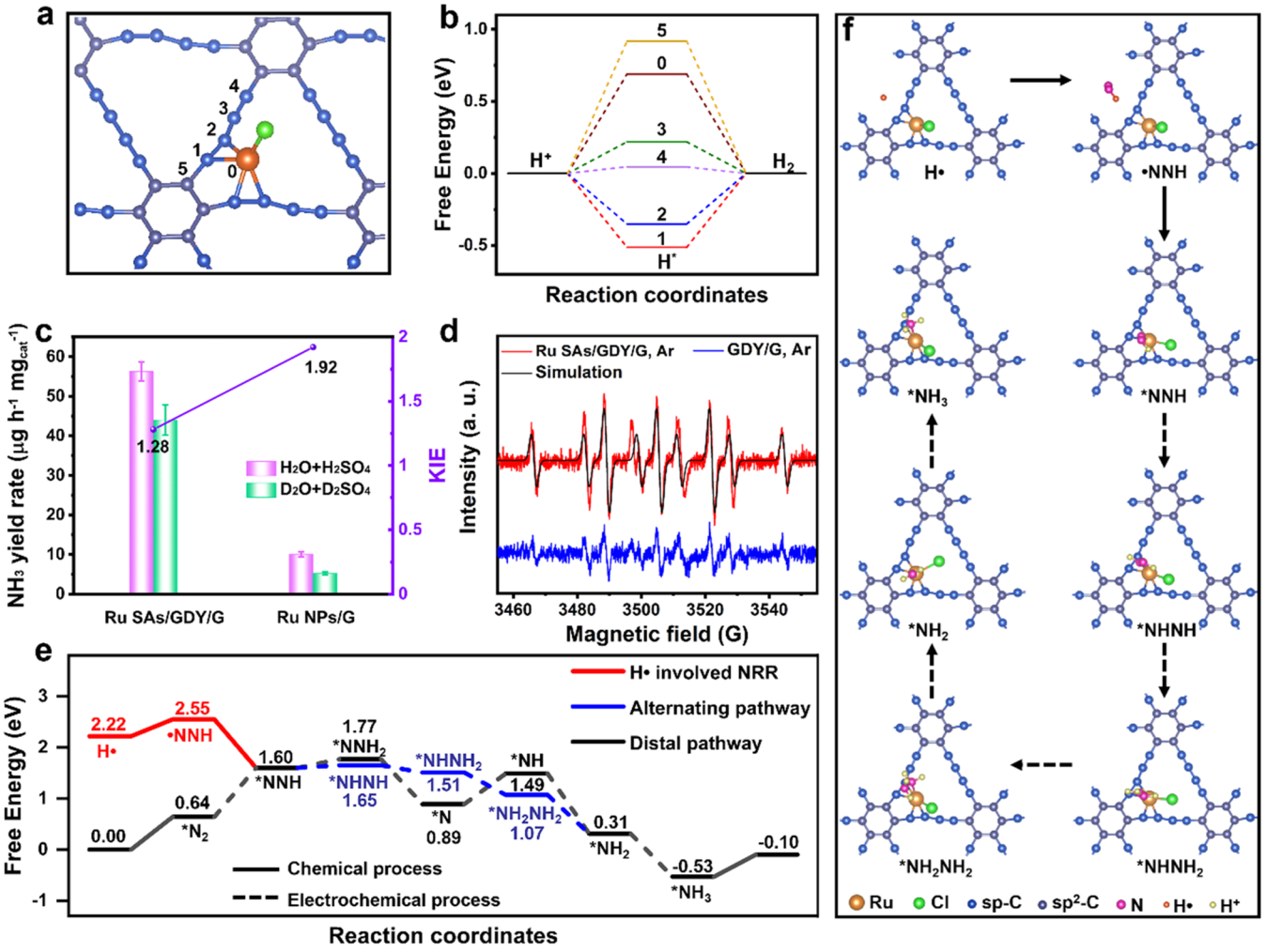

Figure 5. Insights into the mechanism of NRR on Ru SAs/GDY/G. (a) Structure of Ru SAs/GDY/G. (b) Free-energy diagram of the intermediates generated during HER over the Ru SAs/GDY/G at different active sites annotated in panel (a). (c) KIE of H/D and NH_3 yield rates over Ru SAs/GDY/G and Ru NPs/G at −0.1 V. (d) EPR spectra of the solutions obtained after 10 min NRR tests by Ru SAs/GDY/G and GDY/G under Ar. (e) Free-energy diagrams of NRR on Ru SAs/GDY/G. (f) Structure of the intermediates for the H•-involved NRR process.

SAs/GDY/G, revealing the reliability of quantitative tests (Figure 4e and Supporting Figures S30−S32). Moreover, the amount of accumulated NH_3 quantified by spectrophotometric and NMR methods shows a good linear increase with the prolongation of reaction time when $^{14}N_2$ is used (Supporting Figure S33), suggesting the stability of the NH_3 production rate. The enhanced NRR activity of Ru SAs/GDY/G was confirmed by the electrochemically active surface area (ECSA) and electrochemical impedance spectroscopy (EIS) measurement. The ECSA assessed by the double-layer capacitance (C_{dl})[33] is shown in Supporting Figure S34a−c. The determined C_{dl} of Ru SAs/GDY/G and Ru NPs/G is 6.32 and 2.26 mF cm^{-2}, respectively, revealing more exposed active sites for Ru SAs/GDY/G. The charge transfer resistance (R_{ct}) of the Ru SAs/GDY/G is much smaller than that of Ru NPs/G, which could favor charge transfer and thus enhance NRR kinetics (Supporting Figure S34d). The GDY/G possesses a faster charge transfer capacity than GDY, implying that the graphene can not only serve as a template for GDY growth but also improve the conductivity of the catalyst. Furthermore, both the NH_3 yield rate and FE of the Ru SAs/GDY/G exhibit no significant variation through 10 consecutive tests (Figure 4f and Supporting Figure S35). During the long-term electrocatalysis for 600 h at −0.1 V, the current density of the Ru SAs/GDY/G hardly attenuates (Figure 4g). It just shows a trivial loss in the NH_3 yield rate and slight increase in FE after 600 h stability test, confirming the superior electrochemical durability (Figure 4h). Careful examination of TEM, aberration-corrected HAADF-STEM (Supporting Figure S36), EDX (Supporting Figures S37 and S38), Raman and XPS spectra (Supporting Figure S39), and XAS spectra (Supporting Figure S40) displays that the morphology and structure of the Ru SAs/GDY/G remain unchanged after the cycling test, confirming its robustness toward NH_3 synthesis. Importantly, no Ru species in the electrolyte solution are detected after a 600 h stability test on the Ru SAs/GDY/G under −0.1 V, which indicate the excellent stability of Ru single atoms. The above results show that the Ru SAs/GDY/G simultaneously obtains a high FE and NH_3 yield rate, as well as superior stability.

Mechanism of Electrocatalytic NRR. We performed density functional theory (DFT) calculations to further explain the mechanism of NRR on the Ru SAs/GDY/G. The NRR selectivity was also investigated. The predominance of H adsorption over N_2 adsorption is believed to be the main reason for the potential-dependent decrease in NRR

https://doi.org/10.1021/jacs.3c01319
J. Am. Chem. Soc. 2023, 145, 10259−10267

activity.[34,35] Notably, N_2 preferentially adsorbs on the Ru active site compared to the other active sites (Supporting Figures S41 and S42). The H adsorption is significantly suppressed on the Ru active site with a high free-energy change of 0.69 eV, thus effectively suppressing the competitive HER (Figure 5a,b and Supporting Figure S43). To further unravel the mechanism of NRR on Ru SAs/GDY/G, kinetic isotope effect (KIE) experiments were carried out to describe the rate-determining step.[36,37] Figure 5c shows that the NH_3 yield rates of both Ru SAs/GDY/G and Ru NPs/G decrease when the H_2O/H_2SO_4 solvent is replaced by the D_2O/D_2SO_4 solvent. The KIE values of both Ru SAs/GDY/G and Ru NPs/G are greater than 1, indicating that the hydrogenation step is a rate-determining step.[38] Furthermore, the lower KIE value (1.28) of Ru SAs/GDY/G shows excellent proton transfer kinetics compared to Ru NPs/G (1.92), which accelerates the hydrogenation step in NRR. Here, for the first time, we discovered that GDY could generate H$^\bullet$ through *in situ* electron paramagnetic resonance (EPR) technology. 5,5-Dimethyl-1-pyrrolidine-N-oxide (DMPO) as a radical-trapping reagent was tested to rule out the possible interference, and no EPR peaks are observed before the electrochemical test (Supporting Figure S44a). Nine characteristic peaks with an intensity ratio of 1:1:2:1:2:1:2:1:1 are clearly observed for both GDY/G and Ru SAs/GDY/G under an Ar atmosphere at −0.1 V (Figure 5d), which are consistent with the simulation results and are assigned to DMPO-$^\bullet$H (A_N = 22.8 G, A_H = 16.5 G).[39,40] In comparison, no EPR signal obtained for the graphene (Supporting Figure S44b) reveals that the formation of H$^\bullet$ in GDY/G is attributed to GDY. In order to reveal the source of H$^\bullet$, isotope experiments of GDY/G were carried out with a D_2O/D_2SO_4 electrolyte instead of a H_2O/H_2SO_4 electrolyte. The captured signal was assigned to DMPO-$^\bullet$D, with the typical characteristic parameter of A_N = 16.7 G, A_H = 22.7 G, and A_D = 3.5 G, and no EPR peaks corresponding to DMPO-$^\bullet$H are observed, indicating that the hydrogen source of the hydrogen radicals comes from the electrolyte (Supporting Figure S45). The Ru SAs/GDY/G possesses a stronger DMPO-$^\bullet$H signal than that of the GDY/G, whereas Ru NPs/G does not generate H$^\bullet$ (Supporting Figure S46a). When the electrocatalysis is operated under a N_2 atmosphere, the DMPO-$^\bullet$H signal becomes undetectable and the new signal corresponding to $^\bullet NNH_x$ (A_N = 13.9 G, A_H = 8.5 G, and A_N = 1.5 G) is presented for Ru SAs/GDY/G (Supporting Figure S46b), which suggests that the H$^\bullet$ generated by GDY is rapidly consumed to participate in the NRR process. Taken together, the above results indicate that the hydrogenation process of NRR for Ru SAs/GDY/G involves a new mechanism via a H$^\bullet$ transfer pathway. DFT computational studies further confirm the proposed mechanism. As previously reported in the literature, the enzymatic, distal, and alternating pathways are possible mechanisms of NRR.[41] Due to the fact that the N_2 molecule cannot be stabilized as the side-on configuration on the Ru single atom of the Ru SAs/GDY/G, which is suggested by the DFT calculation, the enzymatic pathway is not considered in this work. It shows that the alternating pathway is more favorable than the distal pathway with the optimal end-on adsorption configuration of N_2 (Supporting Figure S42). As shown in Figure 5e, the Ru SAs/GDY/G exhibits a particularly high free-energy change of 0.64 eV, revealing the difficult adsorption of N_2 on its surface. The corresponding first-hydrogenation energy is even higher ($\Delta G_r(^*N_2 \rightarrow ^*NNH)$ = 0.96 eV), indicating that the whole activating process of N_2 is thermodynamically forbidden if only the Ru single atom is involved, which is nevertheless conflict with our experiments. With the assistance of H$^\bullet$, our calculation suggests that the first hydrogenation of the N_2 molecule becomes much easier ($\Delta G_r(H^\bullet \rightarrow {}^\bullet NNH)$ = 0.33 eV). It is obvious that the H$^\bullet$ can effectively activate N_2 to generate $^\bullet$NNH, which is consistent with the captured $^\bullet NNH_x$ in the experimental results (Supporting Figure S46b). Thus, we speculate that the NRR process undergoes a H$^\bullet$ transfer pathway with significantly decreased free-energy gap (Figure 5f). The first step is the activation of the N_2 molecule by H$^\bullet$, giving rise to the $^\bullet$NNH, followed by the exothermic $^\bullet$NNH adsorption (*NNH) on Ru. Subsequently, the stepwise hydrogenation of *NNH occurs through the alternating pathway, which is thermodynamically more favorable than that through the distal pathway (Figure 5f and Supporting Figure S47). Moreover, the hydrogenation of *NNH to *NHNH is the potential-determining step (PDS) of 0.05 eV, which determines the onset potential of NRR.[42] Thus, it can be seen that the corresponding calculated onset potential is −0.05 V, further confirming the superior catalytic activity of NRR toward Ru SAs/GDY/G at −0.1 V. Consequently, the dual-active sites and hydrogen radical-transferring mechanism result in the improved FE and NH_3 yield rate on Ru SAs/GDY/G.

CONCLUSIONS

Our finding demonstrates that Ru SAs/GDY/G is an efficient electrocatalyst for NRR, showing an exceptionally high NH_3 yield rate of 56.8 $\mu g\ h^{-1}\ mg_{cat.}^{-1}$ (4.7 mg $h^{-1}\ mg_{Ru}^{-1}$) and FE of 37.6% at −0.1 V. The experiments and DFT calculations suggest that the Ru single atoms function as active sites for the hydrogenation process of NRR. The GDY not only inhibits H covering on Ru single atoms but also produces H$^\bullet$ to accelerate the kinetics of the hydrogenation process. To our knowledge, the H$^\bullet$-transferring mechanism is a wholly new observation in NRR. Our designed catalysts are conceptually similar, opening new possibilities for the design of highly selective and active electrocatalysts for electrocatalytic hydrogenation reactions.

ASSOCIATED CONTENT

Supporting Information

The Supporting Information is available free of charge at https://pubs.acs.org/doi/10.1021/jacs.3c01319.

Experimental section, construction of models and computation details, structural characterization, photograph of the setup for NRR measurement, additional electrochemical results, and performance comparison (PDF)

AUTHOR INFORMATION

Corresponding Authors

Shuzhou Li − *School of Materials Science and Engineering, Nanyang Technological University, Singapore 639798, Singapore;* orcid.org/0000-0002-2159-2602; Email: lisz@ntu.edu.sg

Lianming Tong − *Center for Nanochemistry, Beijing Science and Engineering Center for Nanocarbons, Beijing National Laboratory for Molecular Sciences, College of Chemistry and Molecular Engineering, Peking University, Beijing 100871, P. R. China;* orcid.org/0000-0001-7771-4077; Email: tonglm@pku.edu.cn

https://doi.org/10.1021/jacs.3c01319
J. Am. Chem. Soc. 2023, 145, 10259−10267

Jin Zhang − *Center for Nanochemistry, Beijing Science and Engineering Center for Nanocarbons, Beijing National Laboratory for Molecular Sciences, College of Chemistry and Molecular Engineering, Peking University, Beijing 100871, P. R. China*; orcid.org/0000-0003-3731-8859; Email: jinzhang@pku.edu.cn

Authors

Xueting Feng − *Center for Nanochemistry, Beijing Science and Engineering Center for Nanocarbons, Beijing National Laboratory for Molecular Sciences, College of Chemistry and Molecular Engineering, Peking University, Beijing 100871, P. R. China*

Jiyuan Liu − *School of Materials Science and Engineering, Nanyang Technological University, Singapore 639798, Singapore*

Long Chen − *College of Environmental Sciences and Engineering, The Key Laboratory of Water and Sediment Sciences (Ministry of Education), Peking University, Beijing 100871, P. R. China*

Ya Kong − *Center for Nanochemistry, Beijing Science and Engineering Center for Nanocarbons, Beijing National Laboratory for Molecular Sciences, College of Chemistry and Molecular Engineering, Peking University, Beijing 100871, P. R. China*

Zedong Zhang − *Department of Chemistry, Tsinghua University, Beijing 100084, P. R. China*

Zixuan Zhang − *Center for Nanochemistry, Beijing Science and Engineering Center for Nanocarbons, Beijing National Laboratory for Molecular Sciences, College of Chemistry and Molecular Engineering, Peking University, Beijing 100871, P. R. China*

Dingsheng Wang − *Department of Chemistry, Tsinghua University, Beijing 100084, P. R. China*; orcid.org/0000-0003-0074-7633

Wen Liu − *College of Environmental Sciences and Engineering, The Key Laboratory of Water and Sediment Sciences (Ministry of Education), Peking University, Beijing 100871, P. R. China*; orcid.org/0000-0002-6787-2431

Complete contact information is available at: https://pubs.acs.org/10.1021/jacs.3c01319

Author Contributions

⊥X.F. and J.L. contributed equally.

Notes

The authors declare no competing financial interest.

■ ACKNOWLEDGMENTS

The authors thank Prof. D. Ma for helpful discussion and L. Wang at Peking University for her help with NMR studies. This work was financially supported by the Ministry of Science and Technology of China (2018YFA0703502 and 2016YFA0200104), the National Natural Science Foundation of China (Grant Nos. 51720105003, 21790052, 52021006, 21974004, and T2188101), the Strategic Priority Research Program of CAS (XDB36030100), the Beijing National Laboratory for Molecular Sciences (BNLMS-CXTD-202001), the China Postdoctoral Science Foundation (Grant Nos. 8206300625 and 8206400103), and the Academic Research Fund Tier 1 (No. RG10/21). The authors thank the computing resources from the National Supercomputing Centre Singapore.

■ REFERENCES

(1) Pang, Y.; Su, C.; Jia, G.; Xu, L.; Shao, Z. Emerging two-dimensional nanomaterials for electrochemical nitrogen reduction. *Chem. Soc. Rev.* **2021**, *50*, 12744−12787.

(2) Guo, W.; Zhang, K.; Liang, Z.; Zou, R.; Xu, Q. Electrochemical nitrogen fixation and utilization: theories, advanced catalyst materials and system design. *Chem. Soc. Rev.* **2019**, *48*, 5658−5716.

(3) Garrido-Barros, P.; Derosa, J.; Chalkley, M. J.; Peters, J. C. Tandem electrocatalytic N_2 fixation via proton-coupled electron transfer. *Nature* **2022**, *609*, 71−76.

(4) Lee, H. K.; Koh, C. S. L.; Lee, Y. H.; Liu, C.; Phang, I. Y.; Han, X.; Tsung, C.-K.; Ling, X. Y. Favoring the unfavored: Selective electrochemical nitrogen fixation using a reticular chemistry approach. *Sci. Adv.* **2018**, *4*, No. eaar3208.

(5) Wang, M.; Liu, S.; Qian, T.; Liu, J.; Zhou, J.; Ji, H.; Xiong, J.; Zhong, J.; Yan, C. Over 56.55% Faradaic efficiency of ambient ammonia synthesis enabled by positively shifting the reaction potential. *Nat. Commun.* **2019**, *10*, No. 341.

(6) Zhu, D.; Zhang, L.; Ruther, R. E.; Hamers, R. J. Photo-illuminated diamond as a solid-state source of solvated electrons in water for nitrogen reduction. *Nat. Mater.* **2013**, *12*, 836−841.

(7) Fang, Y.; Xue, Y.; Hui, L.; Yu, H.; Zhang, C.; Huang, B.; Li, Y. Graphdiyne-Induced Iron Vacancy for Efficient Nitrogen Conversion. *Adv. Sci.* **2022**, *9*, No. e2102721.

(8) Fan, G.; Xu, W.; Li, J.; Chen, J. L.; Yu, M.; Ni, Y.; Zhu, S.; Su, X. C.; Cheng, F. Nanoporous NiSb to Enhance Nitrogen Electroreduction via Tailoring Competitive Adsorption Sites. *Adv. Mater.* **2021**, *33*, No. e2101126.

(9) Wang, J.; Yu, L.; Hu, L.; Chen, G.; Xin, H.; Feng, X. Ambient ammonia synthesis via palladium-catalyzed electrohydrogenation of dinitrogen at low overpotential. *Nat. Commun.* **2018**, *9*, No. 1795.

(10) Schlögl, R. Catalytic synthesis of ammonia-a ″never-ending story″? *Angew. Chem., Int. Ed.* **2003**, *42*, 2004−2008.

(11) Yao, Y.; Wang, H.; Yuan, X.-z.; Li, H.; Shao, M. Electrochemical Nitrogen Reduction Reaction on Ruthenium. *ACS Energy Lett.* **2019**, *4*, 1336−1341.

(12) Liang, X.; Fu, N.; Yao, S.; Li, Z.; Li, Y. The Progress and Outlook of Metal Single-Atom-Site Catalysis. *J. Am. Chem. Soc.* **2022**, *144*, 18155−18174.

(13) Liu, D.; He, Q.; Ding, S.; Song, L. Structural Regulation and Support Coupling Effect of Single-Atom Catalysts for Heterogeneous Catalysis. *Adv. Energy Mater.* **2020**, *10*, No. 2001482.

(14) Fang, S.; Zhu, X.; Liu, X.; Gu, J.; Liu, W.; Wang, D.; Zhang, W.; Lin, Y.; Lu, J.; Wei, S.; Li, Y.; Yao, T. Uncovering near-free platinum single-atom dynamics during electrochemical hydrogen evolution reaction. *Nat. Commun.* **2020**, *11*, No. 1029.

(15) Zhang, Z.; Zhu, J.; Chen, S.; Sun, W.; Wang, D. Liquid Fluxional Ga Single Atom Catalysts for Efficient Electrochemical CO_2 Reduction. *Angew. Chem.* **2022**, *62*, No. e202215136.

(16) Geng, Z.; Liu, Y.; Kong, X.; Li, P.; Li, K.; Liu, Z.; Du, J.; Shu, M.; Si, R.; Zeng, J. Achieving a Record-High Yield Rate of 120.9 μg_{NH3} $mg_{cat.}^{-1}$ h^{-1} for N_2 Electrochemical Reduction over Ru Single-Atom Catalysts. *Adv. Mater.* **2018**, *30*, No. e1803498.

(17) Tao, H.; Choi, C.; Ding, L.-X.; Jiang, Z.; Han, Z.; Jia, M.; Fan, Q.; Gao, Y.; Wang, H.; Robertson, A. W.; Hong, S.; Jung, Y.; Liu, S.; Sun, Z. Nitrogen Fixation by Ru Single-Atom Electrocatalytic Reduction. *Chem.* **2019**, *5*, 204−214.

(18) Gao, Y.; Xue, Y.; Qi, L.; Xing, C.; Zheng, X.; He, F.; Li, Y. Rhodium nanocrystals on porous graphdiyne for electrocatalytic hydrogen evolution from saline water. *Nat. Commun.* **2022**, *13*, No. 5227.

(19) Xue, Y.; Huang, B.; Yi, Y.; Guo, Y.; Zuo, Z.; Li, Y.; Jia, Z.; Liu, H.; Li, Y. Anchoring zero valence single atoms of nickel and iron on graphdiyne for hydrogen evolution. *Nat. Commun.* **2018**, *9*, No. 1460.

(20) Gao, X.; Zhu, Y.; Yi, D.; Zhou, J.; Zhang, S.; Yin, C.; Ding, F.; Zhang, S.; Yi, X.; Wang, J.; Tong, L.; Han, Y.; Liu, Z.; Zhang, J. Ultrathin graphdiyne film on graphene through solution-phase van der Waals epitaxy. *Sci. Adv.* **2018**, *4*, No. eaat6378.

(21) Pan, C.; Wang, C.; Zhao, X.; Xu, P.; Mao, F.; Yang, J.; Zhu, Y.; Yu, R.; Xiao, S.; Fang, Y.; Deng, H.; Luo, Z.; Wu, J.; Li, J.; Liu, S.; Xiao, S.; Zhang, L.; Guo, Y. Neighboring sp-Hybridized Carbon Participated Molecular Oxygen Activation on the Interface of Sub-nanocluster CuO/Graphdiyne. *J. Am. Chem. Soc.* **2022**, *144*, 4942−4951.
(22) Li, J.; Zhong, L.; Tong, L.; Yu, Y.; Liu, Q.; Zhang, S.; Yin, C.; Qiao, L.; Li, S.; Si, R.; Zhang, J. Atomic Pd on Graphdiyne/Graphene Heterostructure as Efficient Catalyst for Aromatic Nitroreduction. *Adv. Funct. Mater.* **2019**, *29*, 1905423−1905431.
(23) Shang, H.; Zuo, Z.; Yu, L.; Wang, F.; He, F.; Li, Y. Low-Temperature Growth of All-Carbon Graphdiyne on a Silicon Anode for High-Performance Lithium-Ion Batteries. *Adv. Mater.* **2018**, *30*, No. 1801459.
(24) Dong, X.-C.; Xu, H.; Wang, X.-W.; Huang, Y.-X.; Chan-Park, M. B.; Zhang, H.; Wang, L.-H.; Huang, W.; Chen, P. 3D Graphene-Cobalt Oxide Electrode for High-Performance Supercapacitor and Enzymeless Glucose Detection. *ACS Nano* **2012**, *6*, 3206−3213.
(25) Ren, H.; Shao, H.; Zhang, L.; Guo, D.; Jin, Q.; Yu, R.; Wang, L.; Li, Y.; Wang, Y.; Zhao, H.; Wang, D. A New Graphdiyne Nanosheet/Pt Nanoparticle-Based Counter Electrode Material with Enhanced Catalytic Activity for Dye-Sensitized Solar Cells. *Adv. Energy Mater.* **2015**, *5*, No. 1500296.
(26) Hu, Y.; Luo, G.; Wang, L.; Liu, X.; Qu, Y.; Zhou, Y.; Zhou, F.; Li, Z.; Li, Y.; Yao, T.; Xiong, C.; Yang, B.; Yu, Z.; Wu, Y. Single Ru Atoms Stabilized by Hybrid Amorphous/Crystalline FeCoNi Layered Double Hydroxide for Ultraefficient Oxygen Evolution. *Adv. Energy Mater.* **2020**, *11*, No. 2002816.
(27) Yu, B.; Li, H.; White, J.; Donne, S.; Yi, J.; Xi, S.; Fu, Y.; Henkelman, G.; Yu, H.; Chen, Z.; Ma, T. Tuning the Catalytic Preference of Ruthenium Catalysts for Nitrogen Reduction by Atomic Dispersion. *Adv. Funct. Mater.* **2019**, *30*, No. 1905665.
(28) Yu, H.; Hui, L.; Xue, Y.; Liu, Y.; Fang, Y.; Xing, C.; Zhang, C.; Zhang, D.; Chen, X.; Du, Y.; Wang, Z.; Gao, Y.; Huang, B.; Li, Y. 2D graphdiyne loading ruthenium atoms for high efficiency water splitting. *Nano Energy* **2020**, *72*, No. 104667.
(29) Yang, J.; Chen, B.; Liu, X.; Liu, W.; Li, Z.; Dong, J.; Chen, W.; Yan, W.; Yao, T.; Duan, X.; Wu, Y.; Li, Y. Efficient and Robust Hydrogen Evolution: Phosphorus Nitride Imide Nanotubes as Supports for Anchoring Single Ruthenium Sites. *Angew. Chem., Int. Ed.* **2018**, *57*, 9495−9500.
(30) Fei, H.; Dong, J.; Arellano-Jimenez, M. J.; Ye, G.; Dong Kim, N.; Samuel, E. L.; Peng, Z.; Zhu, Z.; Qin, F.; Bao, J.; Yacaman, M. J.; Ajayan, P. M.; Chen, D.; Tour, J. M. Atomic cobalt on nitrogen-doped graphene for hydrogen generation. *Nat. Commun.* **2015**, *6*, No. 8668.
(31) Suryanto, B. H. R.; Du, H.-L.; Wang, D.; Chen, J.; Simonov, A. N.; MacFarlane, D. R. Challenges and prospects in the catalysis of electroreduction of nitrogen to ammonia. *Nat. Catal.* **2019**, *2*, 290−296.
(32) Li, X.; Shen, P.; Luo, Y.; Li, Y.; Guo, Y.; Zhang, H.; Chu, K. PdFe Single-Atom Alloy Metallene for N_2 Electroreduction. *Angew. Chem., Int. Ed.* **2022**, *61*, No. e202205923.
(33) Dai, J.; Zhu, Y.; Tahini, H. A.; Lin, Q.; Chen, Y.; Guan, D.; Zhou, C.; Hu, Z.; Lin, H. J.; Chan, T. S.; Chen, C. T.; Smith, S. C.; Wang, H.; Zhou, W.; Shao, Z. Single-phase perovskite oxide with super-exchange induced atomic-scale synergistic active centers enables ultrafast hydrogen evolution. *Nat. Commun.* **2020**, *11*, No. 5657.
(34) Singh, A. R.; Rohr, B. A.; Schwalbe, J. A.; Cargnello, M.; Chan, K.; Jaramillo, T. F.; Chorkendorff, I.; Nørskov, J. K. Electrochemical Ammonia Synthesis-The Selectivity Challenge. *ACS Catal.* **2017**, *7*, 706−709.
(35) Choi, C.; Gu, G. H.; Noh, J.; Park, H. S.; Jung, Y. Understanding potential-dependent competition between electrocatalytic dinitrogen and proton reduction reactions. *Nat. Commun.* **2021**, *12*, No. 4353.
(36) Kong, Y.; Li, Y.; Sang, X.; Yang, B.; Li, Z.; Zheng, S.; Zhang, Q.; Yao, S.; Yang, X.; Lei, L.; Zhou, S.; Wu, G.; Hou, Y. Atomically Dispersed Zinc(I) Active Sites to Accelerate Nitrogen Reduction Kinetics for Ammonia Electrosynthesis. *Adv. Mater.* **2022**, *34*, No. e2103548.
(37) Liu, H.; Lang, X.; Zhu, C.; Timoshenko, J.; Ruscher, M.; Bai, L.; Guijarro, N.; Yin, H.; Peng, Y.; Li, J.; Liu, Z.; Wang, W.; Cuenya, B. R.; Luo, J. Efficient Electrochemical Nitrate Reduction to Ammonia with Copper-Supported Rhodium Cluster and Single-Atom Catalysts. *Angew. Chem., Int. Ed.* **2022**, *61*, No. e202202556.
(38) Fu, H. Q.; Zhou, M.; Liu, P. F.; Liu, P.; Yin, H.; Sun, K. Z.; Yang, H. G.; Al-Mamun, M.; Hu, P.; Wang, H. F.; Zhao, H. Hydrogen Spillover-Bridged Volmer/Tafel Processes Enabling Ampere-Level Current Density Alkaline Hydrogen Evolution Reaction under Low Overpotential. *J. Am. Chem. Soc.* **2022**, *144*, 6028−6039.
(39) Li, J.; Zhan, G.; Yang, J.; Quan, F.; Mao, C.; Liu, Y.; Wang, B.; Lei, F.; Li, L.; Chan, A. W. M.; Xu, L.; Shi, Y.; Du, Y.; Hao, W.; Wong, P. K.; Wang, J.; Dou, S. X.; Zhang, L.; Yu, J. C. Efficient Ammonia Electrosynthesis from Nitrate on Strained Ruthenium Nanoclusters. *J. Am. Chem. Soc.* **2020**, *142*, 7036−7046.
(40) Wang, Y.; Li, H.; Zhou, W.; Zhang, X.; Zhang, B.; Yu, Y. Structurally Disordered RuO_2 Nanosheets with Rich Oxygen Vacancies for Enhanced Nitrate Electroreduction to Ammonia. *Angew. Chem., Int. Ed.* **2022**, *61*, No. e202202604.
(41) Yang, B.; Ding, W.; Zhang, H.; Zhang, S. Recent progress in electrochemical synthesis of ammonia from nitrogen: strategies to improve the catalytic activity and selectivity. *Energy Environ. Sci.* **2021**, *14*, 672−687.
(42) Kim, C.; Song, J. Y.; Choi, C.; Ha, J. P.; Lee, W.; Nam, Y. T.; Lee, D. M.; Kim, G.; Gereige, I.; Jung, W. B.; Lee, H.; Jung, Y.; Jeong, H.; Jung, H. T. Atomic-Scale Homogeneous RuCu Alloy Nanoparticles for Highly Efficient Electrocatalytic Nitrogen Reduction. *Adv. Mater.* **2022**, *34*, No. e2205270.

https://doi.org/10.1021/jacs.3c01319
J. Am. Chem. Soc. 2023, 145, 10259−10267